Alpine hillslope failure in the western US: Insights from the Chaos Canyon landslide, Rocky Mountain National Park USA

Matthew C. Morriss[1], Benjamin Lehmann[2,3], Benjamin Campforts[2,4], George Brencher[5],
Brianna Rick[6,7], Leif Anderson[8], Alexander L. Handwerger[9,10], Irina Overeem[2], and Jeffrey Moore[8]

[1]Earth Sciences Department, University of Oregon Eugene, OR, USA 97403

[2]Institute of Arctic and Alpine Research, Univesrity of Colorado, Boulder, CO, USA

[3]Univ. Grenoble Alpes, Univ. Savoie Mont Blanc, CNRS, IRD, Univ. Gustave Eiffel, ISTERRE 38000 Grenoble, France

[4]Department of Earth Sciences, VU University Amsterdam, Amsterdam, 1081HV, the Netherlands

[5]Civil and Environmental Engineering, University of Washington, Seattle, WA, USA

[6]Department of Geosciences, Colorado State University, Fort Collins, CO 80523, USA

[7]Alaska Climate Adaptation Science Center, Fairbanks, AK, 99775, USA

[8]Department of Geology and Geophysics, Salt Lake City, UT, USA

[9]Jet Propulsion Laboratory, California Institute of Technology, Pasadena, 91109, USA

[10]Joint Institute for Regional Earth System Science and Engineering, University of California, Los Angeles, Los Angeles, CA 90095, USA

Correspondence: Matthew Morriss, PhD (matthew.c.morriss@gmail.com)

Abstract. The Chaos Canyon landslide, which collapsed on the afternoon of June 28th, 2022 in Rocky Mountain National Park presents an opportunity to evaluate instabilities within alpine regions faced with a warming and dynamic climate. Video documentation of the landslide was captured by several eyewitnesses and motivated a rapid field campaign. Initial estimates put the failure area at 66,630 m^2, with an average elevation of 3,555 m above sea level. We undertook an investigation of previous

5   movement of this landslide, measured the volume of material involved, evaluated the potential presence of interstitial ice/snow within the failed deposit, and examined potential climatological forcings at work in causing the collapse of the slope. Satellite radar and optical measurements were used to measure deformation of the landslide in the years leading up to collapse. From 2017 to 2019, the landslide moved ∼5 m yr^{-1}, accelerating to 17 m yr^{-1} in 2019. Movement took place through both internal deformation and basal sliding. Climate analysis reveals the collapse took place during peak snowmelt, and 2022 followed

10   10 years of higher than average positive degree day sums. We also made use of slope stability modeling to test what factors controlled the stability of the area. Models indicate even a small increase in the water table reduces the Factor of Safety to <1, leading to failure. Material volumes were estimated using Structure from Motion (SfM) models incorporating photographs from two field expeditions on July 8th, 2022 – 10 days after the slide. Detailed mapping and SfM models indicate ∼ 1,258,000 ± 150,000 m^3 of material was deposited at the slide toe and ∼1,340,000 ± 133,000 m^3 of material was evacuated from the

15   source area. Our holistic approach to the collapse of the Chaos Canyon landslide provided an opportunity to examine a landslide that may be representative of future dynamic alpine topography, wherein failures becomes more common in a warming climate.

1   Introduction

The Chaos Canyon collapse took place during a sunny early-summer day at 3:31 PM local time on June 28th, 2022 in Rocky
Mountain National Park (RMNP), Colorado, USA (Fig. 1). The event was first reported through social media from bystanders
situated at Lake Haiyaha (Fig. 1) and directly beneath the slide. These social media posts resulted in a rapid response from Earth
scientists who sought to investigate: 1) the causes of collapse; 2) the mechanisms triggering this collapse - such as a landslide,
the collapse of a rock glacier or the role of cryogenic processes in general, and 3) the amount of material mobilized by the
collapse. More broadly, this investigation developed through a desire to understand whether this failure is part of the global
trend toward cryosphere instability and the degradation of permafrost conditions driven by climate change (Geertsema et al.,
2022; Patton et al., 2019). Mass movements in alpine regions have been documented with increasing frequency in the European
Alps, Canada, and Alaska (Dai et al., 2020; Geertsema et al., 2022; Lacroix et al., 2022); however, few such observations have
been made in the continental United States. RMNP was visited by ∼4.4 million people in 2021, making it the 14th most visited
National Park in the US (NPS, 2022). As the climate warms, developing awareness around future alpine hazards within RMNP
and across the broader western U.S. Cordillera is an important priority.

1.1   Stability of alpine topography

A warming climate has led to a warming of permafrost, glacier retreat, and growing instability in alpine regions across the globe
(Patton et al., 2019; Shan et al., 2014). An increase in rock fall, landslides, and glacier instability has been well documented
in the European Alps and the alpine regions of Canada and Alaska (Cossart et al., 2008; Deline et al., 2021; Kos et al., 2016;
Geertsema et al., 2022). Some of these events have received international news coverage (e.g. areas below the Planpincieux
glacier in Italy on the flanks of Mont Blanc) and resulted in intermittent area closures and evacuations (Dematteis et al., 2021;
Giordan et al., 2020). Other events have been more remote and garnered interest from the scientific community but have not had
an impact on a broader population (e.g. Lipovsky et al., 2008). So far, few notable increases in instabilities in the alpine regions
of the conterminous United States have been reported. It remains to be seen whether mountainous terrain in the conterminous
US will experience a similar increase in events like those seen in Alaska and the European Alps. The current geomorphological
evolution of these alpine environments integrates both (1) the long-term response (i.e. on scales of 1-10 ka) to glacial retreat
and glacial conditioning of the topography, and (2) the recent impact of a changing climate (i.e. on time scales of 10-100 years)
via glacier retreat and permafrost degradation (Huggel et al., 2010; Stoffel and Huggel, 2012). Quantifying the dynamics
of mountain landforms facing climate change is proving difficult and predictions of the geomorphological response such as
mountain slope instability to future climate scenarios remain limited because the processes involved operate on interdependent
timescales and are therefore difficult to characterize. Herein, we seek to both develop the tools necessary to analyze those
events and understand the stability of similar alpine slopes within a warming climate regime by characterising the relation
between permafrost, topographic and climate forcings, and slope instabilities.
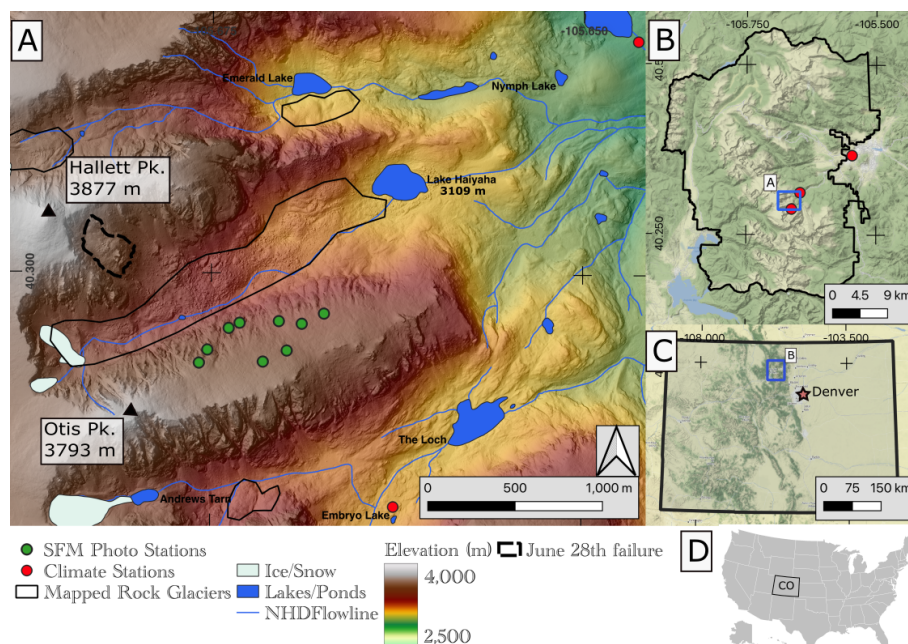
Figure 1. Overview of landslide area. **A)** Hillshade with hypsometric tint from 1 m lidar Digital Elevation Model (DEM) of the Chaos Canyon landslide and surrounding topography. Highlighted are the outlines of mapped rock glaciers (Johnson et al., 2021); the nine photo locations used in the structure from motion survey, and the two climate stations used in climate reconstructions for the slide. Lakes, streams, and ice/snow bodies are from the National Hydrography Dataset (NHD) (USGS, 2019) **B)** The location of panel **A** within Rocky Mountain Park. **C)** The location of panel **B** within Colorado, USA **D)** The location of Colorado (panel **C**) within the USA

.

1.2 The Chaos Canyon landslide

50 The Chaos Canyon landslide took place above treeline in the alpine reaches of Rocky Mountain National Park. The pre-failure landslide extended from ∼3450 m to ∼3660 m in elevation. The landslide itself is a diamicton composed of grains ranging from fine sediments to large boulders (∼10s of m). The slide occurred along the contact between the Middle Proterozoic Silver Plume Granite and the early Proterozoic biotite schists (Fig. A1) with a moderate foliation dipping to the southeast and toward Chaos Canyon (Braddock and Cole, 1990). The deposit in the bottom of Chaos Canyon was mapped by Braddock and
55 Cole (1990); Johnson et al. (2021) as a potentially active rock glacier, with the landform that failed on June 28th mapped as Quaternary talus (Figs. 1, A1).

1.3 Primary Questions

This collapse spurred a series of questions at the scale of the landslide itself which also broaden to the scope of alpine landforms across the conterminous United States:

60   1. Was the landslide moving prior to its collapse on June 28th ?

  2. What were the climatic factors that led to the collapse?

  3. Can we constrain the volume of the slide? What is this volume?

  4. Can we ascertain the presence or absence of permafrost? Is there evidence of degradation of permafrost through time?

  5. Can we use slope stability modeling to further evaluate the rheology of the slide and gain insights into the processes at
65   work? For instance, can we quantify the role of groundwater?

  6. What does this work tell us about the other landforms and their stability across the park and western Cordillera which is
     rapidly warming?

2   Methods

To answer questions posed above, we undertook a multidisciplinary investigation of the Chaos Canyon landslide and the events
70 that led up to the failure. We combined both satellite-based image correlation using optical data and interferometric synthetic
aperture radar (InSAR) to constrain movement of the landslide prior to June 28th, 2022. A climatological analysis examined
the role of snowmelt and whether the timing of the collapse coincided with peak snowmelt. To assess the landscape evolution
impacts of the landslide, we created a SfM model. We further developed climatological analysis by modeling the potential
presence of permafrost or interstitial ice within the landform. Finally, we conducted a slope stability analysis to evaluate the
75 potential factors at play in the stability of the deposit prior to collapse.

2.1   Remote sensing

To understand the processes at work leading up to and during the June 28th collapse in Chaos Canyon, it is important to investi-
gate characteristics of landslide motion prior to collapse. As in-situ survey data are unavailable, we utilized two complementary
remote sensing techniques: InSAR and image correlation.

80 **2.1.1   InSAR**

InSAR is a remote sensing technique that can be used to measure millimeter-scale displacement of the ground surface from
space (Bürgmann et al., 2000). Interferograms are InSAR-derived maps containing information about surface displacement
between two acquisition times along the satellite line-of-sight (LOS). To investigate rates of displacement of the landslide
prior to the collapse on June 28th, we created interferograms using data acquired by the Copernicus Sentinel-1 A/B satellites.
85 Specifically, we processed and analyzed all possible short temporal-baseline ($\leq$24 days) Sentinel-1 interferograms overlapping
the study area from July 15th-September 15 of 2015-2021 using the Jet Propulsion Laboratory InSAR Scientific Computing
Environment version 2 software (Rosen et al., 2012). Short temporal baselines were chosen to limit possible unwrapping
errors during interferogram processing, which are frequently caused by features moving more than half the radar wavelength

(~2.8 cm for Sentinel-1) between acquisitions. Stacks of 34, 35, and 42 interferograms were derived from ascending (satellite

90 flight north and looking east) track 78, ascending track 151, and descending (satellite flying south and looking west) track 56, respectively. Interferograms were processed with 6 looks in range and 1 look in azimuth, resulting in roughly 14 by 14 m pixel spacing. A 2017 U.S. Geological Survey (USGS) 3DEP Digital Elevation Model (DEM) with 10 m pixel spacing was used to remove the topographic component of the phase and geocode the interferograms. For each of our three interferogram stacks, we removed low quality and noisy interferograms using a coherence threshold >0.6. Coherence is related to the similarity of

95 scatterers in the images that form interferograms; low coherence indicates that the target surface is changing appreciably and displacement signals are unreliable. We lastly computed the pixel-wise median where coherence was >0.4, yielding a single median velocity map for each track (e.g., Fig. 3).

2.1.2   Image correlation

We used image correlation to measure 2D ground displacements (east-west and north-south) at the Chaos Canyon landslide

100 based on Google Earth and PlanetScope images. We examined all available historical Google Earth images of the site and identified two high-resolution photos that had little snow coverage and no visible artifacts. The images selected were from 9/2016 and 8/2019. Before exporting the images, we turned off terrain and 3D effects, as well as image compression and filtering. We selected the maximum available image output resolution of 8192 x 4925 pixels from Google Earth Pro. Scaling of the images from pixels to meters had to be manually evaluated; for this we measured several distances on each image in

105 Google Earth and then determined the corresponding pixel dimensions, resulting in a scaling value of 0.21 m/pixel. We then applied a Fast Fourier transform-based image correlation approach that first aligns the image pair with a co-registration routine, then evaluates internal misalignments using a moving window to measure displacements in the plane of image (Bickel et al., 2018). We used a window size of 256 x 256 pixels with 50% overlap, resulting in ~27 m resolution outputs, and a vector based post-processing filter (for details see Bickel et al., 2018).

110 In addition, we calculated the time-dependent displacement of the landslide between 2017 and 2021 using PlanetScope imagery (3 m pixel resolution). We selected 5 images acquired during the snow-free period (either from August or September each year). Unfortunately, there were no snow-free images in 2022 prior to the failure of the slope. The PlanetScope images are orthorectified and have radiometric, geometric, and sensor corrections applied (Team, 2017). We performed image correlation on 10 image pairs with a minimum time span of ~1 yr and a maximum time span of ~4 yrs between images (Table A1).

115 For image correlation analysis using PlanetScope imagery, we used the Outlier-Resistant Correlator (OR-Corr) subpixel image correlation method (Milliner and Donnellan, 2020). We used a 33 x 33 pixel correlation window with a step size of 9 pixels, resulting in 27 m pixel resolution displacement maps. We then used the MintPy timeseries software (Yunjun et al., 2019) to invert for the time-dependent motion of the landslide.

2.2   Climate analysis

120 To better understand the climatic circumstances of the June 28th collapse, we analyzed the records at the Bear Lake SNOw-pack TELemetry Network (SNOTEL), from the United States Department of Agriculture and Natural Resources Conservation

Service, 2022) located ∼3 km to the northeast of the landslide. Specifically, we wanted to test the hypothesis that snowmelt may have contributed to the catastrophic failure. We extracted the Bear Lake Climate SNOTEL (Fig. 1) temperature record going back to 1991 (NRCS, 2023). This meteorological site is located at 2903 m above sea level (asl). We made use of the

125 Global Historical Climatology Network site (USR0000CEST) located in Estes Park at 2382 m asl (Fig. 1) to determine a local environmental lapse rate of 4.65×10^{-3} °C m^{-1}. We then shifted the temperature record collected at Bear Lake to reflect the environment at the top of the slide at ∼3147 m asl. We made a cumulative positive degree day sum (PDDS) of the temperature record representative of conditions at the top of the slide (Braithwaite and Hughes, 2022). By applying a global average ablation rate of ∼4.5 mm day^{-1} °C^{-1} (Anderson et al., 2014), we estimated spring snowmelt atop the Chaos Canyon landslide.

130 ## 2.3 Structure From Motion

A DEM of the affected area, after the June 28th collapse, was obtained using SfM and terrestrial photogrammetry. Data collection took place on July 8, 2022, ten days after the collapse. Photographs were taken from 9 different stations on the East of Otis Peak ridge providing a direct view of the landslide (Fig. 1; Table A2). Photo acquisition was made between 10:30 and 15:00 ensuring ideal light conditions. We used a Sony Alpha a7S III Mirrorless Digital Model with a Tamron 28-200mm

135 f/2.8-5.6 Di III RXD Lens mounted on a tripod. The following settings were used for all pictures: a focal length of 8.0, iso 400, zoom of 70 mm and shutter time between 1/800 and 1/1250 s. Pictures were taken with approximately 80% of overlap between each other. The coordinate of each station was recorded using a handheld GPS (Garmin GPSmap 64s). This post-collapse DEM was compared to a reference DEM (before the event) to (i) record the new geometry of the area and (ii) quantify the amount of erosion and deposition involved. The reference 1 m DEM is provided by the USGS program National Map 3DEP and was

140 acquired in 2017.

The 3D point cloud was created with Agisoft Metashape Professional using 305 photographs. The photographs were first aligned with high accuracy, setting the key point limit to 4000 and the tie point limit to 100,000. The resulting sparse point cloud was filtered using a reconstruction uncertainty criterion of 300. The camera locations were estimated with a total error of 40 m (X error of 22.1 m, Y error of 10.3 m and Z error of 31.7 m). We used the reference 1-meter DEM from USGS to

145 create virtual Ground Control Points (GCP; Fig. 2). Those GCPs were chosen outside and around the landform affected by the destabilization, on bedrock features that are recognizable on both the reference DEM and the photographs acquired after the event. This approach produced 5 GCPs with total location error of about 0.7 m (X error of 0.04 m, Y error of 0.09 cm and Z error of 0.13 cm, see Table A3). Finally, we produced a dense cloud made of 20×10^6 points that we converted into a DEM of 0.26 m/pixel resolution with a point density of 14 points/m^2. Irregularities in the obtained DEM were further removed using the

150 following sequence of steps. First, an iterative procedure was used to identify all local depressions in the DEM (Barnes et al., 2014). These were subsequently filled using an Inverse Distance Weighing algorithm. This step was repeated until all local minima were removed. In a second step, positive spikes in the DEM were identified using a slope-based DEM-filter. These spikes were subsequently removed and resulting gaps were interpolated using the iterative procedure described above. Then the smoothed post-collllapse DEM was subtracted from the pre-collapse DEM (2017) to construct a DEM of difference (DoD),

155 from which volumes of erosion and deposition can be calculated.
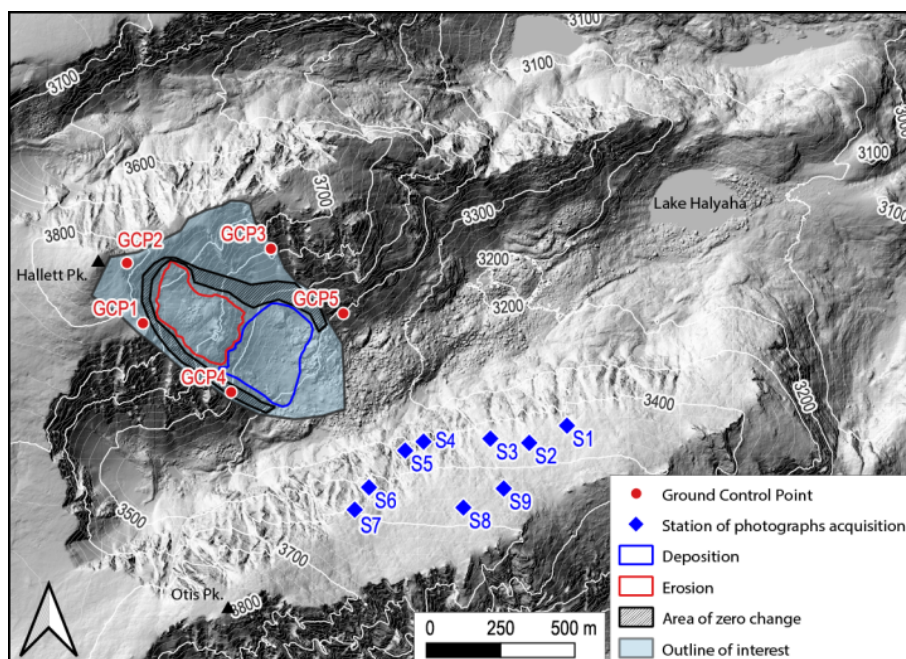
Figure 2. Location of the stations where the photographs where acquired (S) and the ground control points (GCP) used to create the post-collapse DEM. Hillshade and elevation lines were computed using the 1-meter DEM provided by the USGS program National Map 3DEP and acquired in 2017. Areas of erosion and deposition were derived from differencing the 2017 DEM and our July 8th SfM DEM

2.4 Permafrost modeling

To explore the soil and bedrock temperature profile at the time of the June 28th collapse, we used a coupled model of snow and permafrost, consisting of an empirical snow model (ECsimplesnow) and the Geophysical Institute Permafrost Laboratory (GIPL) (Brown et al., 2003; Jafarov et al., 2012; Overeem et al., 2018). GIPL is a one-dimensional heat flow model, simulating
160 ground temperature evolution and the depth of the active layer by solving non-linear heat equations with phase change. GIPL is often set up as a spatial grid consisting of adjacent columns; however, we have little information on the soil and debris cover thickness or spatial variability in snow depth. Therefore, we chose to model the annual evolution of subsurface temperature for a single vertical column.

We initialized subsurface properties needed for the GIPL model with soil characteristics from global soil data released in
165 SoilGrid (Hengl et al., 2014). Key properties include soil texture and water content. We had no in-situ data, but the pre-collapse satellite imagery indicated an existing diamicton – consisting of sediment and boulders. For our simulations, we assumed ∼30 cm regolith soil, 2.7 m debris and coarse, un-weathered sediment, and bedrock beyond that depth. Coarse-grained sediment and bedrock then define the frozen and unfrozen thermal conductivity and heat capacity according to relationships established from laboratory experiments (Goodrich, 1982; Kersten, 1949; Schaefer and Jafarov, 2016).

170   We ran the combined model over the 2022 water year (October 1,2021 to September 30, 2022), with a time-series of daily air temperature and precipitation, as extrapolated from observations at the Bear Lake station (as described in Section 2.2). Soil or bedrock temperatures were strongly modulated by snow cover over winter, due to its low thermal conductivity (Zhang, 2005). The effect is complex, and ground temperature can either be lower or higher than the snow surface or air temperature, depending upon the timing, duration, and thickness of the seasonal snow cover and the air temperature history. The spatially variable but

175 locally large wind-drifted snow accumulations in cirques in the Rocky Mountains act as a thermal insulator on an annual basis. Our regional snow model, from original empirical parameterization of Brown et al. (2003), used daily precipitation input over the water year and combined this with a snow classification map (Sturm et al., 1995) to establish snow thickness and density. This is numerically implemented in the ECsimplesnow model and coupled with the GIPL model. The landslide sits between~3450 m and ~3660 m a.s.l., which is well above the regional tree line, so vegetation coverage was set to be 'open

180 terrain', meaning that trees or extensive shrubs do not impact the snow properties.

2.5   Slope stability modeling

To explore the conditions that led to collapse of the deposit, we used the limit equilibrium analysis (e.g., Duncan, 1996) program Slide2 (Rocscience, 2021). For the analyses, we imported pre-collapse topography based on the LiDAR DEM of Rocky Mountain National Park. To estimate the boundary between the pre-collapse deposit and the underlying bedrock we

185 extrapolated a surface under the pre-collapse deposit based on known bedrock outcrops on either side of the post-collapse deposit in QGIS. The underlying bedrock topography was estimated by adjusting contours, converting the contours to point data, and then re-rasterizing the data using the *GDAL_rasterize* command in QGIS.

    Slide2 was used for the limit equilibrium analysis. Because the collapse occurred during the snow melt season, we explored the stability of the pre-collapse deposit to changes in water table depth. Material properties were tuned based on our knowledge of the site from in-situ observations, pre-collapse velocity data, and permafrost modeling. We assume a Mohr-Coulomb failure

190 criteria for the pre-collapse deposit and underlying bedrock (Labuz and Zang, 2012). We compared the pre-collapse global minimum factor of safety in cases with and without a slight rise in local water table. The factor of safety is the ratio of resisting forces and driving forces (e.g., Duncan, 2000). When the factor of safety is greater than 1 the slide is stable; when the factor of safety is less than one the slide will fail. The specific details of the model domain are described below.

    In Slide2, we added a shear plane between the deposit and bedrock. We also included a change in material properties between

195 the landslide and underlying bedrock (density 2000 kg m^{-3} for the deposit and 2700 kg m^{-3} for the bedrock). We then tuned the properties of the shear plane and deposit to represent a global minimum factor of safety slightly greater than 1 (actual FoS of 1.037) to represent the observed condition that the landslide was moving prior to collapse (see 3.1.2) we hypothesized this indicates a well developed shear plane developed (Fig. 10). For the shear plane, we assume a cohesion of 1 kPa and a friction angle of 30°, while for the ice-cemented deposit we assume cohesion of 250 kPa and a friction angle of 50°. To simulate the

200 effects of a rising water table due to snow melt we added a water table surface 1 m above the shear plane (Rocscience, 2021).

3 Results

3.1 Pre-collapse movement

3.1.1 InSAR

205 For all tracks, median coherence within the landslide boundaries was low (0.36 ± 0.17 for ascending track 78, 0.37 ± 0.16 for ascending track 151, and 0.52 ± 0.16 for descending track 56, Fig. 3D). Twelve wrapped interferograms from ascending tracks 78 and 151 show clear evidence of landslide displacement beginning in August 2015 (Figs. 3B, A2A, A3). Median LOS velocities in the landslide were not distributed in a manner consistent with cohesive downslope displacement. Instead, we observed patches of apparent upslope and downslope LOS velocity, along with patches of apparently stable area, are scattered

210 across the landslide surface in no clear pattern, which is a due to unwrapping errors caused by the high deformation gradient (Figs. 3B, A2A, 5). Thus, the median velocity does not provide a reliable indicator of landslide activity. By comparison, for all tracks, a rock glacier in the cirque to the north has a more spatially consistent downslope velocity signal (Fig. 3B), while rocky, flat areas above and below the landslide appear mostly stable outside of topography-correlated atmospheric noise.

3.1.2 Image Correlation

215 #### 3.1.3 Google Earth

Results of Digital Image Correlation (DIC) analysis are shown in Figure 4. We observe a broad area of relatively large-magnitude displacement corresponding to the top surface of the landslide: in the $\sim$3 years (i.e. the period 2016 - 2019) between images this area moved on average 10.5 ± 0.5 m (Fig. 4B). Maximum displacements of 11.5 m were found on the northern portion of the slide surface. The main landslide body showed southeast trending movement with consistent displacement

220 vectors (Fig. 4C). Areas of low correlation between images, and those which were filtered in post-processing, were located in the region covered by snow in the 2019 image (Fig. 4A) and near the toe of the slope (Fig. 4B). We also observed an adjacent movement near the northern head of the landslide with lower magnitude displacements ($\sim$2 m) and more southerly oriented movement than the main body. Here it appears that a portion of the talus adjoining the main slide body is moving in response to motion of the main slide away from its toe. A visible scarp had developed in the 2019 image at the head of this smaller

225 sliding body. The mean displacement azimuth for the main slide body is 117 degrees clockwise from north, while the smaller northern portion is moving at an azimuth of 162 degrees. Finally, movement detected on and at the toe of the steep frontal slope has similar orientations only slightly lower magnitude than at the crest ($\sim$8 m). This may indicate evidence supporting a basal sliding mechanism for slide movement, that together with some amount of internal shear could generate the displacement pattern measured (Fig. 4B).

230 We can assess uncertainty in our image correlation results by measuring estimated movements in stable areas not anticipated to experience movement in the period between image acquisitions. For this, we evaluate a portion of the results on the broad south slopes of Hallet Peak, and find that resolved mean movements are 0.3 ± 0.1 m, well below the measured displacement
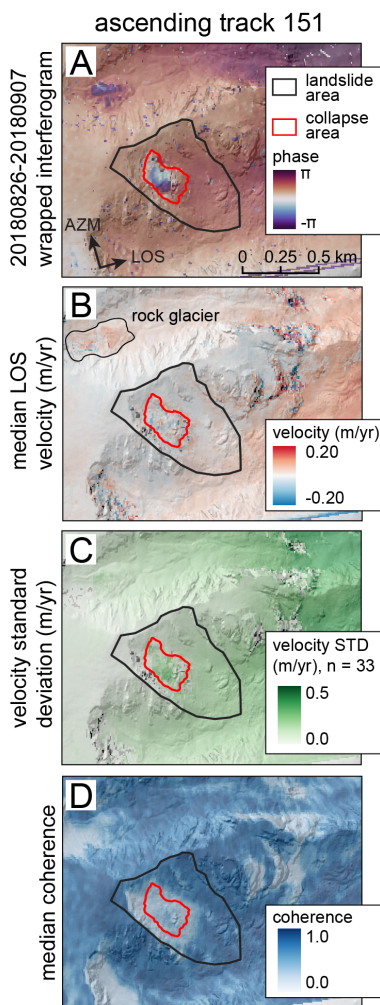
Figure 3. InSAR-derived LOS velocity of the landslide prior to the June 28th collapse. Interferograms come from Sentinel-1 ascending track 151. **A)** A wrapped interferogram from the summer of 2018 showing clear landslide deformation of roughly 10 cm in 12 days. **B)** Median LOS velocity of the failure area and landslide area. Interferograms with short temporal baselines and high median coherence on the landslide slope were used to create the velocity map. Positive values (red) correspond to motion away from the satellite along the satellite LOS. Note the spatial inconsistency of signals within the landslide. Negative velocity values at lower elevations are caused by topography-correlated atmospheric noise. **C)** Standard deviation of LOS velocity. **D)** Median coherence of the failure area and landslide area.

of the landslide. While the image comparison shows significant displacement of the landslide between 2016 and 2019, no information is available from this analysis on when this movement might have occurred during the interval. Finally, while the relative displacements are robust, our use of Google Earth imagery requires empirical scaling assessment done on a case-by-case basis and not benefiting from the pixel dimension information or metadata from the original acquisition. This leads to
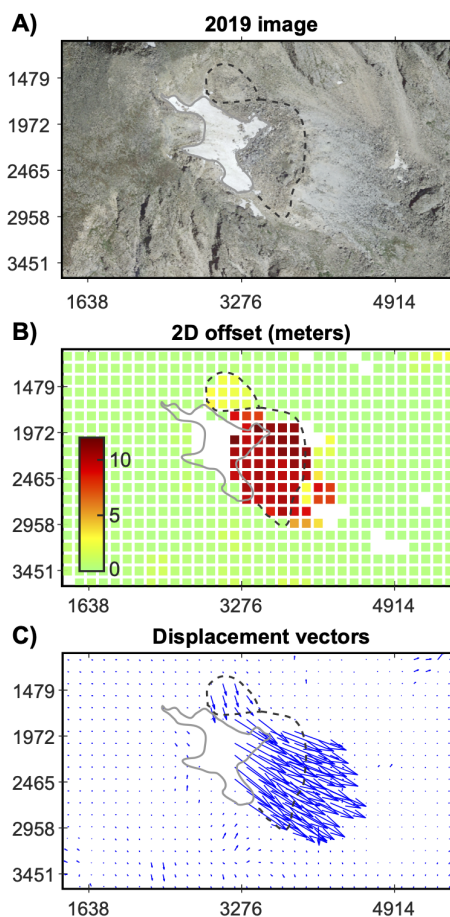
Figure 4. Results of digital image correlation for the Chaos Canyon landslide comparing © Google Earth imagery from 9/2016 and 8/2019. **A)** 2019 photo of the slide with snow patch highlighted (grey solid line). Dashed lines highlight the crest of the main slide as well as a smaller adjoining slide thought to be secondary in response to undermining. **B)** Scaled 2D offset magnitude. Blank cells are areas omitted during filtering; these mostly occur in snow-covered areas and at the toe of the steep frontal slope. Movement of the main body is 10.5 m on average. **C)** Displacement vectors. The main Chaos Canyon slide and secondary adjoining slide show different displacement magnitude and orientation (dashed lines repeated from **A**). Coordinates are pixels in east (x) and north (y) orientations.

some uncertainty in the absolute scaling of the displacement magnitudes. However, given consistent scaling measurements across the images, together with visibly displaced boulders that can be measured on Google Earth, we feel confident that the results are reasonably accurate and can be interpreted quantitatively.
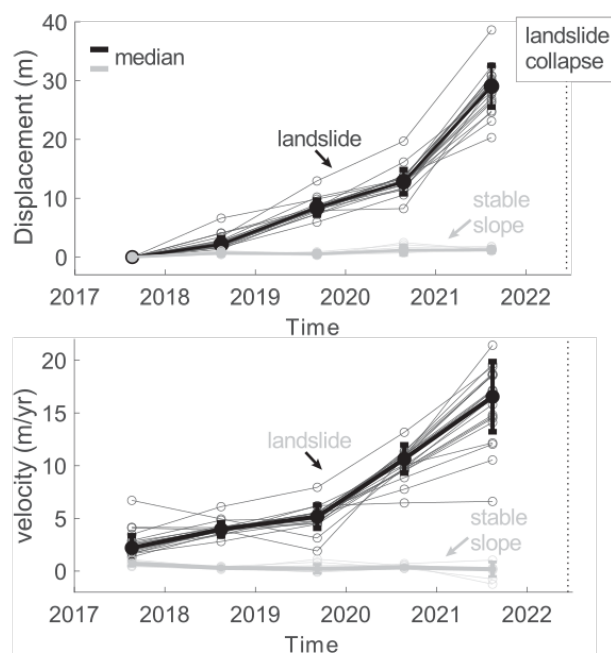
Figure 5. Image correlation results from Planet images taken in 2017, 2018, 2019, 2020, and 2021. **A)** The horizontal displacements of every pixel mapped within the landslide. The black line is the mean displacement with 1-σ bars. The gray line shows the same statistic but for stable areas outside the landslide. A greater sampling of Planet images reveals increasing displacements moving toward the present. **B)** The mean and 1-σ uncertainty envelopes of velocity and for the landslide (black) and pixels examined outside of the footprint of the landslide (gray). The pixels outside the landslide show no systematic movement, as compared with the accelerating landslide.

3.1.4 PlanetScope

Image correlation of the PlanetScope imagery is in general agreement with the spatial extent and magnitude of the actively deforming slope measured with the Google Earth imagery (Section 3.1.3). Our time series analysis reveals that the landslide moved as a coherent unit but exhibited different rates spatially. The median cumulative displacement of the landslide was ~29 m $\pm$ 3.5 m ($\pm$ standard deviation) between 2017 and 2021. The maximum cumulative displacement was ~39 m and the minimum was ~20 m. The velocity increased monotonically between 2017 and 2021, but exhibited a distinct acceleration point starting in the summer of 2019. The median velocity across the landslide was <5 m/yr prior to 2019 and then increased to ~17 m/yr by 2021. This change in kinematics starting in the summer of 2019 suggests a change in stability conditions of the slope. We also assessed the uncertainty by examining the apparent movement in a stable area. We found that the stable slope exhibited apparent displacements < 1.3 m $\pm$ 0.27. We also explored the 1/velocity relationship often used to predict landslide failure (e.g. (Fukozono, 1990; Voight, 1989), but found it yielded poor results. We did not pursue this line of inquiry further.
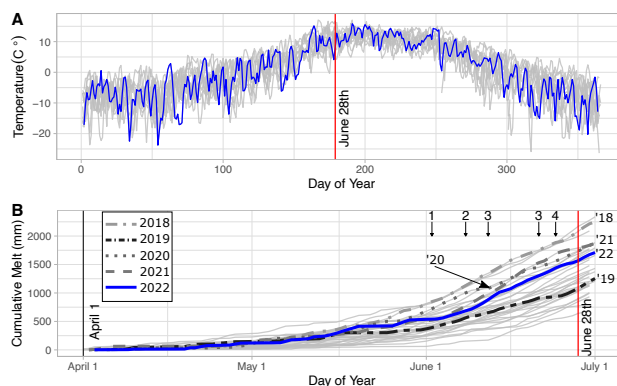
Figure 6. Climate analysis of the Chaos Canyon landslide. **A)** The mean daily temperature series estimated for ∼3668 m or the elevation at the top of the slide. 2022 is highlighted blue. 1990 thru 2021 temperature series are gray lines. The collapse occurred on June 28th. **B)** The calculated cumulative snowmelt for the past 32 springs. 2022 is the blue line with 1990-2021 snowmelt seasons shown in gray. Inset numbers highlight dates for frames from Planet Imagery in Figure 7. The snowmelt curves for the previous four years (2018, 2019, 2020, and 2021) are also highlighted.

3.2 Snowmelt Rates

Our detailed climate analysis shows that the Chaos Canyon landslide collapsed as average daily temperatures were increasing to their summer peak ∼21 days later (Fig. 6A). 2022 was not out of the ordinary from previous years over the last three decades. It was not remarkably warmer than past years in the winter months, nor were spring temperatures significantly warmer than typical. However, the temperature series does indicate that the collapse may have taken place as warming increased the rate of snowmelt. This observation is further supported by the cumulative snowmelt we calculated at the elevation equivalent with the top of the landslide (Fig. 6B). Snowmelt begins in April with melt increasing rapidly after June 1. Compared with the 1990-2021 seasons, 2022 had slightly higher melt than most of the previous 32 years, with the 11th highest calculated melt April - July 1. These calculations indicate that the collapse took place during the peak snowmelt for the spring season (Fig. 6B). This is bolstered by the Planet imagery in Figure 7. Panel A, June 2nd through June 24th, show a significant decrease in snow extent across the landslide in clear accordance with the snowmelt calculates in Figure 6B.

3.3 Change detection

The obtained difference map is shown in Figure 8. This map was used to delineate erosion and deposition zones for the collapse. Delineation of these zones was done based on regions of zero surface change (green areas) between before and after event elevation data. Towards the edges of Figure 8 some artefacts start to appear in the data which can be attributed to lower point densities used during the SfM procedure in the boundary areas.

Uncertainty of the post-collapse DEM is obtained by calculating the Root Mean Squared Error (RMSE) between the reference LiDAR DEM and the post-event DEM for a region surrounding the erosion and deposition features that were minimally
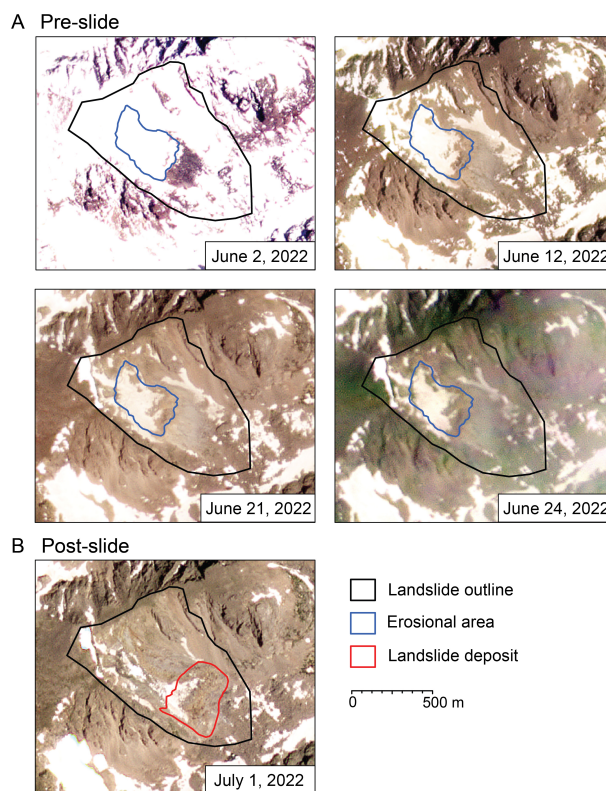
Figure 7. Planet imagery of upper Chaos Canyon in the days preceding the collapse. **A Pre-collapse** Images dates are denoted in Figure 6B. Both temperature modeling and satellite imagery indicate the failure took place during a period of rapid snowmelt. **B Post-collapse)** The final deposit after the June 28th collapse is highlighted. Pieces of the permanent snowpatch have been translated with the landslide. Imagery thanks to Team (2017).

disturbed (visually determined in the field). The RMSE equals 2.39 m for this region, a value that is used to estimate uncer-

270 tainty ranges on total erosion and deposition volumes. The erosion area covers 55,639 m^2 and experienced an average erosion of 24.09 $\pm$ 2.39 m or a corresponding volume of 1,340,000 $\pm$ 133,000 m^3. The deposition area covers 64,477 m^2 and experienced an average deposition of 19.52 $\pm$ 2.39 m or a corresponding volume of 1,258,000 m^3 $\pm$ 154,000 m^3. Erosion and deposition volumes are similar within uncertainty ranges. The deposited volume is slightly lower than the eroded volume which could be due to errors during the SfM DEM production or because of sediment evacuation towards downstream areas during

275 and following the event.

3.4 Permafrost modeling

The steep front of the pre-failure landslide averages an $\sim40^{circ}$ slope, greater than a typical angle of repose could be indicative of interstitial ice holding the deposit together (Carson, 1977; Whalley and Martin, 1992). Further investigation of the potential
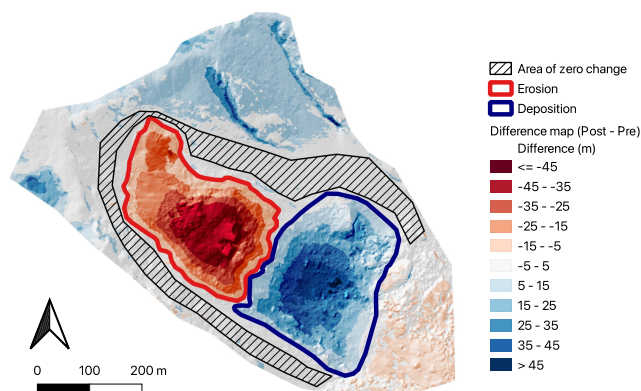
Figure 8. DEM of difference between Post and Pre-event topography. Negative values indicate erosion (red colors), positive values indicate deposition (blue colors), green values indicate regions of zero change. The dashed area indicates a regions where no visible change took place during the event and was used to calculate the accuracy of the DEM.

for interstitial ice through ground temperature modeling indicates that permafrost conditions persist to at least 15 m depth in the pre-collapse deposit (Fig. 9). For the 2021-2022 model year minimum simulated surface temperatures was -4 °C, maximum simulated surface temperature was 16 °C, and the mean surface temperature was 2 °C. For transient simulations through the 2021-2022 water year the thaw front propagated to 0.96 cm depth by June 28th 2022, the date of failure. These results are only relevant for the portions of the pre-collapse deposit that were snow free. The deepest the simulated thaw front reaches, i.e. the maximum active layer depth, is ~1.85 m at the end of the hydrological year in October (Figs. 9, A4).

3.5 Slope stability modeling

To explore the role of snow melt as a potential trigger of the landslide, we simulated a slight rise in the water table within the pre-collapse deposit. We expect that a basal shear plane is well developed at the base of the pre-collapse deposit, because the landslide has been accelerating and has undergone large displacements (Figs. 4,5). The inclusion of this water table reduced the resistive forces in the system leading to a global minimum factor of safety of 0.995 and thus failure of the landslide. The pre-collapse deposit thus appears to be highly sensitive to a reduction of normal stress associated with a rising water table, likely associated with spring snow melt.
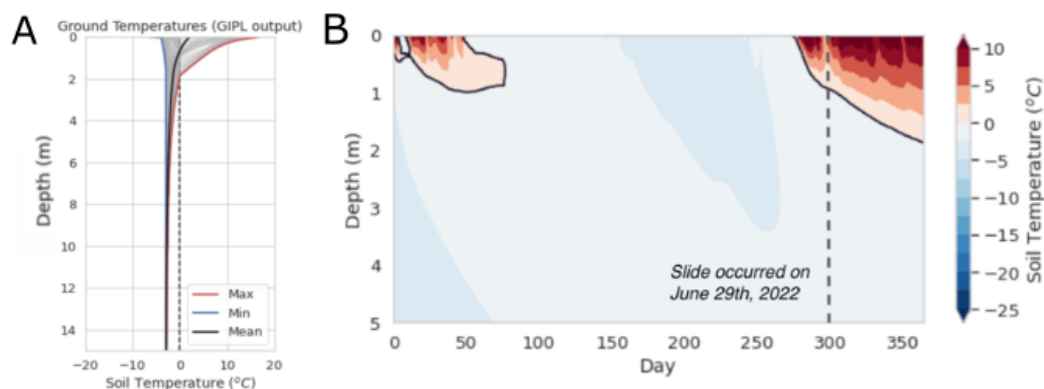
Figure 9. Simulation results of the combined snow and soil temperature model over the water year *Oct 2019-Oct 2020*. **Panel A.** Shows soil temperature as a function of depth, with even maximum temperatures below ∼2 m depth never reaching above 0°C. **Panel B.** Shows soil temperatures with depth at the Chaos Canyon landslide across a single water year. This result mirrors the depth of the active layer shown in **A.**
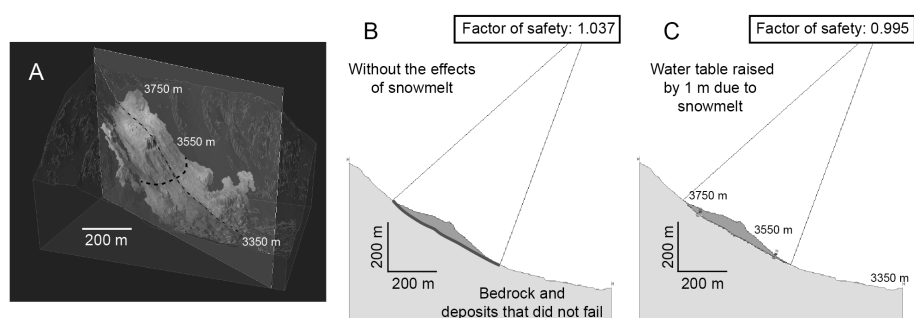
Figure 10. Output from limit equilibrium slope stability analysis. **A)** View of the pre-collapse topography in three-dimensions. The pre-collapse deposit is shown in red, yellow, and blue. The thick dashed line represents the lower edge of the deposit that failed which is also shown in B and C. The thin dashed line shows the cross section also shown in B and C. **B)** Limit equilibrium analysis showing the global minimum slip surface and factor of safety for the simulated pre-slide deposit (purple) using the program Slide2. The failure surface (see the red line) is located at the transition between the purple body that moved during the collapse and the underlying material. **C)** Limit equilibrium analysis showing the global minimum slip surface and factor of safety for the simulated pre-collapse deposit with the effects of a water table 1 m above the contact between the pre-collapse deposit and the underlying bedrock.

4   Discussion

Rapid environmental change is predicted to increase the occurrence of landslides and rock failures in high, alpine terrain. Nevertheless, few alpine rock failures have been documented in conterminous United States. The Chaos Canyon landslide
295   affords insights on the role of mass wasting in alpine terrain through abundant field and remotely sensed data as well as

numerical scenario modeling. In the following, we discuss changes leading up to the event that could serve as tools to monitor future landscape stability.

4.1 Pre-collapse movement and potential causes of the June 28th collapse

The June 28th collapse of the Chaos Canyon landslide appears to have been an event lacking a well documented modern
300 analogue in alpine regions of the conterminous United States. Image correlation results provide evidence of accelerating pre-collapse displacement at least as early as summer 2017, suggesting that unstable conditions developed over the course of years as opposed to within a single spring season (Figs. 4, 5). It is important to note that inconsistencies in InSAR-derived median LOS velocities over the surface of the landslide suggest that our short-baseline interferograms suffered from unwrapping errors. This interpretation is consistent with median LOS velocities of more than 0.93 cm/day during July 15th-September 15th
305 of 2015-2021. Henceforth, we only discuss displacement rates derived from our image correlation efforts.

Initial rates of horizontal displacement were slow at ∼5 m/yr between 2017 and 2019, but the landslide rapidly accelerated after 2019 to a moderate rate of ∼17 m/yr (for velocity classes see: Cruden and Varnes, 1996). We identified no clear climatological forcing that led to the acceleration in 2019; however, there is the potential for a progressive weakening of the failure surface beneath the landslide (Eberhardt et al., 2016) and/or potential slip localization to a single shear plane (Viesca and Rice,
310 2012; Scuderi et al., 2017). Both of these phenomena suggest through continued and repeated movement of the landslide, the landslide weakens and accelerates until its ultimate catastrophic failure. Similar behavior, wherein increases in sliding velocity result in weakening of the failure surface, has been modeled to occur in fault zones (Ito and Ikari, 2015). Given that the Chaos Canyon landslide has several years of slow and then accelerating movement, it is a strong candidate for further analysis of potential rate weakening.

315 We cannot, with available datasets, ascertain when this pre-failure movement initiated; however, we can refer to the long-term trend in temperature to evaluate the potential impacts of a warming climate on this alpine landslide. Temperature trends at the top of the landslide, approximated from the Bear Lake SNOTEL, show a clear warming signal across the past three decades (Fig. 11A, B), with a consistent positive temperature anomaly after 2009. Warming temperatures have been documented to correspond to landslides in both high elevation and high latitude landscapes, particularly where permafrost or ground ice is
320 present (e.g., Cossart et al., 2008; Deline et al., 2021; Patton et al., 2019). Increased temperatures lead to permafrost thaw and decrease slope stability through either a change in the physical conditions of the slope (e.g., reduced cohesion) or hydrologic conditions (e.g., increased pore pressure and hydrologic conductivity; Patton et al., 2019).

The presence of permafrost conditions (Fig. 9) in the pre-collapse deposit opens the possibility that ice occupied interstitial spaces between clasts (Kenner et al., 2017; Eriksen et al., 2018). If a continuous ice layer was present within the pre-collapse
325 deposit, snowmelt may have been channeled to locations where tension cracks were present through the pre-collapse deposit. If abundant interstitial ice was present, then the entire pre-collapse body may have been moving down slope due to internal deformation and sliding. Satellite imagery of the steep front of the pre-slide deposit suggests that ice was exposed there in gullies; additionally, the pre-slide front was steeper than the angle of repose, indicating the presence of internal ice (Carson, 1977; Whalley and Martin, 1992). However, the lack of observed ice in the post-failure deposit suggests that interstitial ice
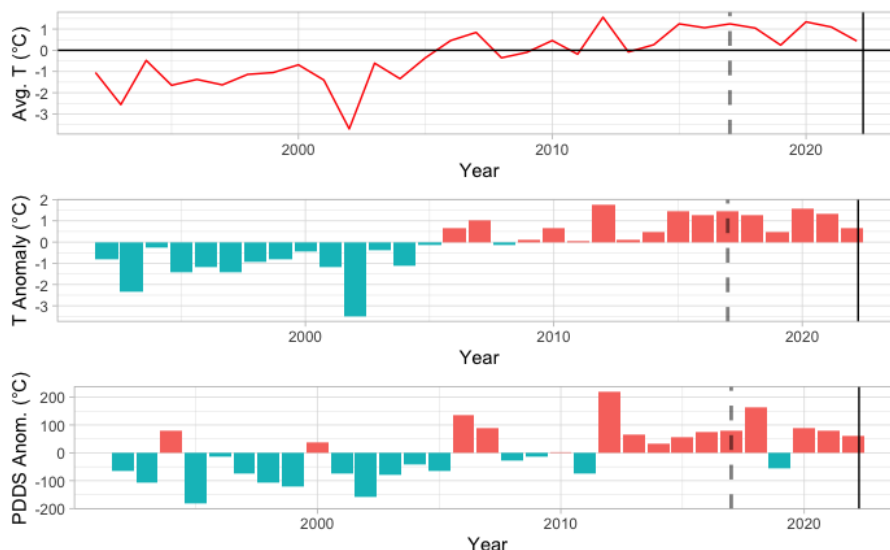
Figure 11. Temperature trends across the top of the Chaos Canyon landslide, using the Bear Lake SNOTEL record and the calculated local lapse rate. **Panel 1)** Average annual temperature from 1991 to the 2022 clearly shows a warming trend that begins in 2006. **Panel 2)** The annual Temperature anomaly from the 31 year average, cooler colors correspond to a negative anomaly, warmer colors a positive anomaly. Here, the warming is even more visible as a positive temperature anomaly consistent across every year after 2009. **Panel 3)** The PDDS anomalies calculated for the first 6 months of the calendar year for the past 31 years at the slide elevation (Braithwaite and Hughes, 2022). While the PDDS anomalies show more fluctuation than the other indicators, after ∼ 2012 the PDDS is mostly greater than in the preceding 21 years. Moreoever, PDDS has been directly linked with snowmelt and is a closer proxy to potential melt that could penetrate the slide mass. The gray dashed line is the first date of image correlation data, and the dark black line is the failure date of the Chaos Canyon slide.

330 may not have been abundant, though internal heating during the slide could have also melted any internal ice (Pudasaini and Krautblatter, 2014). Further model simulations should explore the interaction between percolating melt water and permafrost within the pre-slide deposit, to determine the potential for the presence of interstitial ice through the pre-slide body.

We hypothesize that permafrost within the slide deposit became increasingly warm due to the changing climatic conditions within Chaos Canyon over the last ∼30 years, likely reducing the stability of the landform. Coincident with warming tem-

335 peratures, we observed an increasing rate of horizontal displacement of the landslide over the past five years, with evidence suggesting both basal sliding and internal deformation (Figs. 4, 5). The thawing permafrost, combined with internal deformation and some surface cracking (Fig. 4), may have provided an increased availability of flowpaths for snowmelt and rain to penetrate into the slide mass, increasing the hydrostatic pressure and promoting destabilization of the deposit on June 28th (Figs. 6B, 10, 11C; Bogaard and Greco, 2016).

4.2 Landslide characterization

To compare the Chaos Canyon landslide to other landslides, we used a few common metrics that also inform landslide rheology and process. Landslide mobility is commonly expressed using the ratio between the maximum length of the sediment travel path (L) and the difference between the highest and lowest point impacted by the landslide (H) (Geertsema et al., 2009). The L/H ratio is a useful metric in hazard assessment because it indicates how far downstream landslide derived material can reach from any given source area (Iverson et al., 2015). Several studies have also shown a positive relation between the volume of mobilized material (V) and the mobility index (L/H). A compilation of some global mobility indices versus landslide volumes is given in Figure 12A. The Chaos landslide has a mobility value of L/H $\approx$ 1.8 and fits within ranges of earlier documented rockslides of similar volumes (Fig. 12A). The total inundated area of the Chaos landslide (m^2) also follows earlier documented trends between landslide extent and volume (Fig. 12B). An alternative mobility index for landslides is calculated as $A/V^{2/3}$. The mobility coefficient for the Chaos landslide of $A/V^{2/3} \approx 10$ being at the lower end of earlier documented mobility values of high-mobility landslides (Griswold and Iverson, 2008). Landslides with very high mobility coefficients are debris flows on ice or landslides in very wet environments where basal liquefaction plays a role (e.g. the OSO landslide where $A/V^{2/3}$; Iverson et al., 2015). The lower value of $A/V^{2/3}$ for the Chaos landslide indicates a limited mobility where ice and water probably played a minor role in controlling landslide runout. However, this doesn't mean that the changes in internal ice and water were not potential contributory factors to the June 28th collapse. Perhaps this landslide would have been more mobile if it had collapsed prior to the observed warming we document (Fig. 11) which was likely paired with a decrease in interstitial ice.

4.3 Ramifications for alpine landscape evolution

We are witnessing a transformative period in alpine landscapes (Patton et al., 2019). The past several decades have seen changes to the ice glaciers of the world (e.g. Kääb et al., 2018), the slopes adjacent to retreating glaciers (e.g. Dai et al., 2020), rock glaciers (e.g. Bodin et al., 2017), and permafrost (Patton et al., 2019). We have shown evidence that the Chaos Canyon landslide falls within this spectrum of alpine landscape with instabilities likely tied to a warming climate (Fig. 11). Our change detection methods reveal the slide translated $\sim$ 1,258,000 $\pm$ 150,000 m^3 of material downslope. Moreover, the downstream effects on water quality in Lake Haiyaha (Fig. 1) and other portions of the catchment continue to be investigated by other scientists. What we captured as part of this study is active landscape evolution, a process likely to be replicated in other alpine catchments.

The conditions documented in Chaos Canyon, an east-facing deglaciated valley which experiences higher rates of snow accumulation due to wind redistribution, are not unique in the Rocky Mountains. Where possible, mass movements should be inventoried and monitored for changing displacement rates, such as those observed in Chaos Canyon, as an indicator of a potentially impending slope failure for safety monitoring and hazard mitigation. We particularly recommend these assessments in popular recreation areas throughout the mountain west, such as the National Parks. We demonstrate the utility of image correlation and the potential challenges of InSAR to detect mass movements, with repeat surveys serving to assess change over time. We caution other investigators to take a combined methods approach – if possible – pairing image correlation
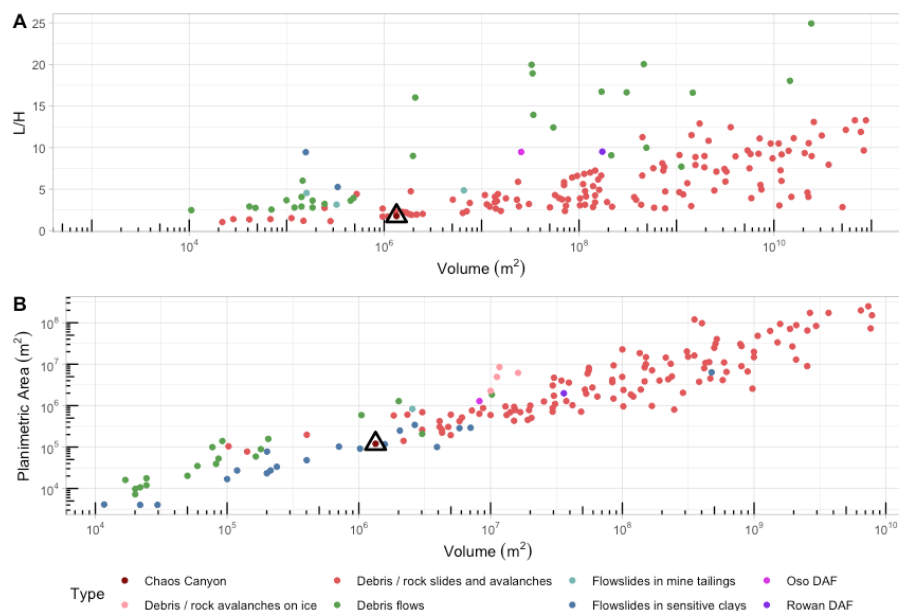
Figure 12. Landslide mobility indices. **Panel A.** The commonly used maximum landslide travel path (L) over landslide height (H) versus landslide volume. The Chaos Canyon landslide (marked as red dot with black triangle) has a low L/H ≈ 1.8. and falls within the field of other debris slides, rock slides, and rock avalanches (Iverson et al., 2015). **Panel B.** The Chaos Canyon landslide inundated an area consistent with power law relationship between landslide area and volume discussed in Griswold and Iverson (2008).

with InSAR to ensure rapidly deforming landforms are properly detected and their movement quantified with more than one method. Additionally, given the role of permafrost thaw in slope destabilization, a broader effort to model, inventory, and

375   monitor areas of permafrost across the Rocky Mountains would be beneficial. Locations where steep slopes, identified mass movements, and permafrost intersect need further monitoring to assess future hazards – particularly in areas with large numbers of visitors. There were luckily no injuries or casualties reported with the Chaos Canyon landslide, but the increasing popularity of hiking, climbing, and other alpine activities place more people in potentially dangerous locations. It is therefore imperative to understand how and where alpine slope instabilities may occur to minimize hazards in a warming world.

380   **5   Conclusions**

The June 28th, 2022 Chaos Canyon landslide provides a unique opportunity to understand rapid landscape changes in the alpine environments of the Rocky Mountain west. Moreover, the event took place in the 14th most visited National Park in the country. Through our investigations, we have shown that the landslide, which translated ∼ 1,258,000 ± 150,000 m³, was moving up to 17 m/yr in years prior to the June 28th, 2022 failure, and was likely moving through a mix of both basal-sliding

385   and internal deformation. These rates of translation were fast enough to cause unwrapping errors in our InSAR observations. With an L/H mobility metric of ≈ 1.8, the Chaos Canyon landslide could be characterized as a debris slide, rockslide, or rock

avalanche, meaning the landslide had limited mobility upon collapse. The slide occurred during the peak of spring snowmelt, and the preceding years were particularly warm compared with the 31 year running average. Moreover, the first six months of the calendar year across the past 31 years have shown higher than average positive degree days, likely impacting the timing and

390   rate of snowmelt. As we documented through slope stability modeling, even a small increase in the water table leads to slope failure. We characterize the Chaos Canyon landslide as part of the broader alpine landscape evolution occurring across the high elevation and high latitude regions of the globe, and recommend the inventorying and monitoring of such alpine landscapes to better understand where these types of hazardous slope failures may be likely to occur under a warming climate.

Code availability.   The code developed and associated with this publication is published on Zenodo. https://doi.org/10.5281/zenodo.7854068.

395   Other pre-existing and published tools are referenced in the text with sufficient detail for methods replication.

Code and data availability.   The code developed and associated with this publication is published on Zenodo. https://doi.org/10.5281/zenodo.7854068.

Video supplement. A short .mp4 video file of Planet images between 2017 and 2022 of the landslide is available in the Supplementary

400   Material.
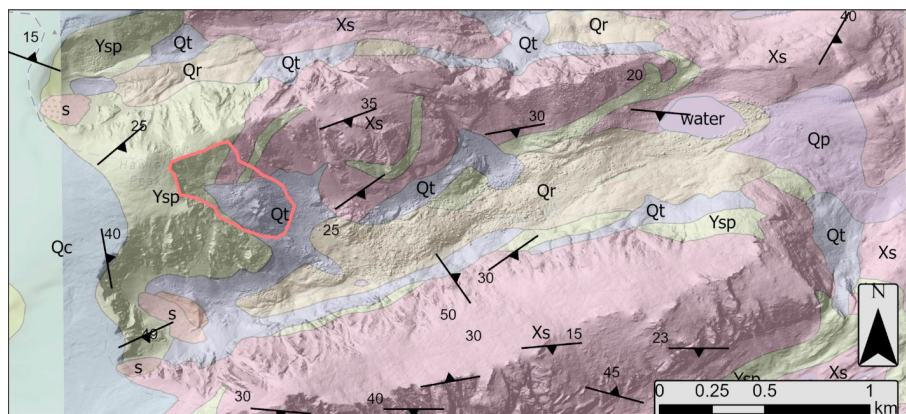
Figure A1. Geologic context of the Chaos Canyon landslide, perched above the canyon floor atop a contact between the Silver Plume Granite (Ysp) and a Biotite schist. There is also a foliation dip toward Chaos Canyon. Underlying geologic data is from (Braddock and Cole, 1990)
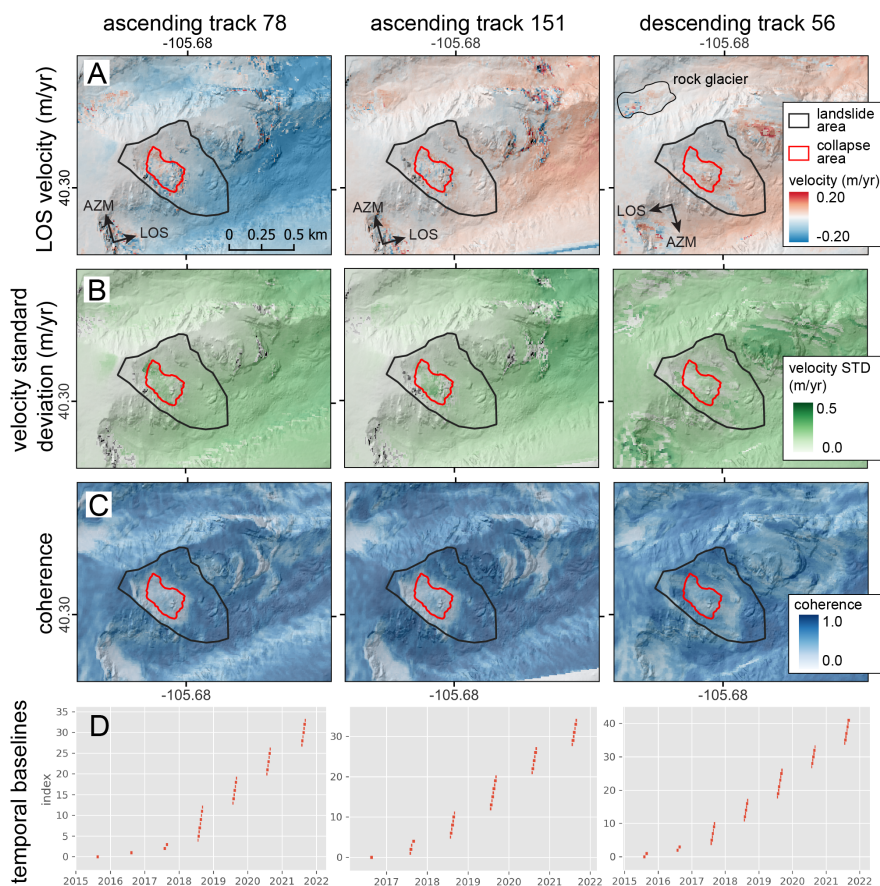
Figure A2. InSAR-derived median LOS velocity of the landslide feature prior to catastrophic failure. Sentinel-1 interferograms from ascending track 78, ascending track 151, and descending track 56 with short temporal baselines and high median coherence on the landslide slope were used to create each velocity map. **A)** Median LOS velocity of the landslide feature and surrounding area. Positive values (red) correspond to motion away from the satellite along the satellite LOS. Note the spatial inconsistency of signals within the landslide. Apparent topography-correlated displacements are caused by atmospheric noise. **B)** Standard deviation of median LOS velocity. **C)** Median coherence of the landslide feature and surrounding area. Coherence is related to the similarity of scatterers in the images that form our interferograms. Note the low coherence over the landslide feature, which indicates that the surface of the feature is changing appreciably. **D)** Temporal baselines of all available 6, 12, and 24-day Sentinel-1 interferograms from late summer. Each bar spans the temporal baseline of a single interferogram, beginning and ending at the primary and secondary acquisition dates.

Table A1. Planet image pairs used in image correlation.

Image Pairs	Start Date	End Date	Number of Days
0	9/3/17	8/29/18	360
1	9/3/17	9/21/19	748
2	9/3/17	9/6/20	1099
3	9/3/17	8/28/21	1455
4	8/29/18	9/21/19	388
5	8/29/18	9/6/20	739
6	8/29/18	8/28/21	1095
7	9/21/19	9/6/20	351
8	9/21/19	8/28/21	707
9	9/6/20	8/28/21	356
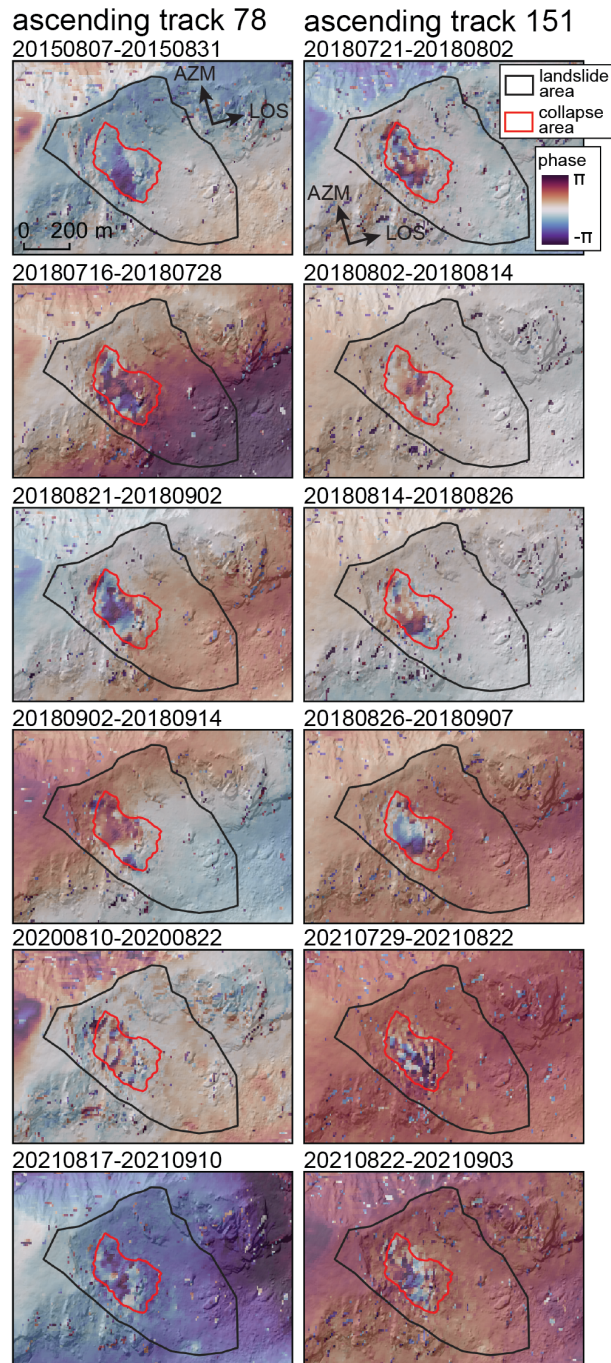
Figure A3. Wrapped short-baseline interferograms showing clear evidence of landslide displacement. Displacements of more than twice the radar wavelength, shown here, result in errors during unwrapping. Displacement signal is not as clear in other interferograms due to strong atmospheric noise and/or low coherence of the moving area. (left) Interferograms from ascending track 78. (right) Interferograms from ascending track 151.
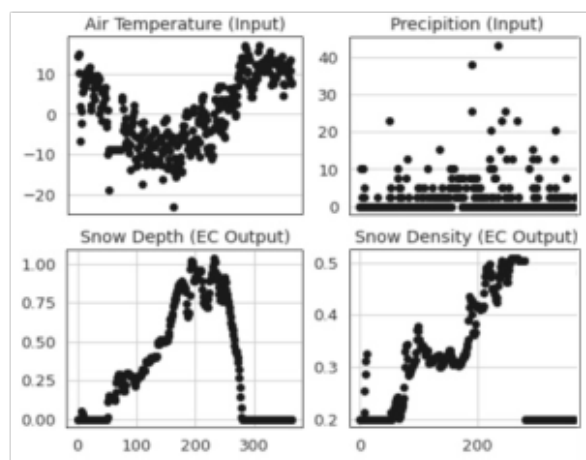
Figure A4. Simulation results of the combined snow and soil temperature model over the water year *Oct 2019-Oct 2020*. Daily air temperature and precipitation inputs are derived from correcting/extrapolating the lower elevation meteorological station at Bear Lake, RMNP. Snow depth and density are modeled by the snow model and are subsequent input for the GIPL heat conduction model.

Table A2. Coordinates of the stations where the photographs were acquired.

Station ID	x coord.	y coord.	z coord. (m a.s.l.)
1	105°40.044′	40°17.8760′	3462
2	105°40.1335′	40°17.8441′	3471
3	105°40.2262′	40°17.8517′	3443
4	105°40.3847′	40°17.8460′	3447
5	105°40.4287′	40°17.8296′	3452
6	105°40.5145′	40°17.7625′	3547
7	105°40.5481′	40°17.7219′	3594
8	105°40.2899′	40°17.7264′	3576
9	105°40.1936′	40°17.7611′	3547

Table A3. Ground Control Point X, Y, Z, and Total errors in cm and error in SfM model px.

Label	X error (cm)	Y error (cm)	Z error (cm)	Total (cm)	Image (pix)
GCP1	0.387	-12.626	17.858	21.874	10.849 (46)
GCP2	-3.810	2.052	-19.821	20.288	13.109 (49)
GCP3	7.790	8.976	9.717	15.352	4.105 (68)
GCP5	-5.117	-9.542	-6.412	12.584	2.211 (91)
GCP4	0.686	11.160	-1.124	11.237	3.680 (48)
Total	4.517	9.589	13.028	16.795	7.296

Author contributions. Each author played a key role in this research project. MM guided the research from the start by bringing together the group and scheduling meetings and drafting this manuscript. He also contributed the climate analysis. BL and BC contributed the SfM modeling and change detection analysis - as well as the metrics of landslide mobility. GB and AH contributed the Insar and planet Image correlation analysis. BR contributed to the discussion editing of the final manuscript. LA contributed the slope stability modeling and aided MM in the climate analysis and permafrost modeling. AH contributed the Planet image correlation and aided the InSAR efforts. IO contributed the permafrost modeling. JM added the Google Earth based digital image correlation. All authors contributed to the editing of this manuscript.

Competing interests. The authors declare that they have no conflict of interest

Acknowledgements. The first author would like to thank Dr. Harrison Gray (USGS) for sending the initial video of this landslide posted to Twitter that spurred this research to action. Part of this research was carried out at the Jet Propulsion Laboratory, California Institute of Technology, under a contract with the National Aeronautics and Space Administration (80NM0018D0004). We would also like to thank the support of the French ANR-PIA funding program (ANR-18-MPGA-0006). We also thank the developers of the Digital Image Correlation code we implemented with Google Earth Imagery https://github.com/bickelmps/DIC_FFT_ETHZ.

References

Anderson, L. S., Roe, G. H., and Anderson, R. S.: The effects of interannual climate variability on the moraine record, Geology, 42, 55–58, https://doi.org/10.1130/G34791.1, 2014.

Barnes, R., Lehman, C., and Mulla, D.: Priority-flood: An optimal depression-filling and watershed-labeling algorithm for digital elevation models, Computers & Geosciences, 62, 117–127, https://doi.org/10.1016/j.cageo.2013.04.024, 2014.

Bickel, V. T., Manconi, A., and Amann, F.: Quantitative assessment of digital image correlation methods to detect and monitor surface displacements of large slope instabilities, Remote Sensing, 10, https://doi.org/10.3390/rs10060865, tex.article-number: 865, 2018.

Bodin, X., Krysiecki, J.-M., Schoeneich, P., Le Roux, O., Lorier, L., Echelard, T., Peyron, M., and Walpersdorf, A.: The 2006 Collapse of the Bérard Rock Glacier (Southern French Alps): The 2006's Collapse of the Bérard Rock Glacier, Permafrost and Periglacial Processes, 28, 209–223, https://doi.org/10.1002/ppp.1887, 2017.

Bogaard, T. A. and Greco, R.: Landslide hydrology: from hydrology to pore pressure, WIREs Water, 3, 439–459, https://doi.org/10.1002/wat2.1126, _eprint: https://onlinelibrary.wiley.com/doi/pdf/10.1002/wat2.1126, 2016.

Braddock, W. and Cole, J.: Geologic Map of Rocky Mountain National Park and Vicinity, Colorado, USGS Numbered Series 1973, U.S. Geological Survey, 1990.

Braithwaite, R. J. and Hughes, P. D.: Positive degree-day sums in the Alps: a direct link between glacier melt and international climate policy, Journal of Glaciology, pp. 1–11, https://doi.org/10.1017/jog.2021.140, 2022.

Brown, R. D., Brasnett, B., and Robinson, D.: Gridded North American monthly snow depth and snow water equivalent for GCM evaluation, Atmosphere-Ocean, 41, 1–14, https://doi.org/10.3137/ao.410101, 2003.

Bürgmann, R., Rosen, P. A., and Fielding, E. J.: Synthetic Aperture Radar Interferometry to Measure Earth's Surface Topography and Its Deformation, Annual Review of Earth and Planetary Sciences, 28, 169–209, https://doi.org/10.1146/annurev.earth.28.1.169, _eprint: https://doi.org/10.1146/annurev.earth.28.1.169, 2000.

Carson, M. A.: Angles of repose, angles of shearing resistance and angles of talus slopes, Earth Surface Processes, 2, 363–380, https://doi.org/10.1002/esp.3290020408, _eprint: https://onlinelibrary.wiley.com/doi/pdf/10.1002/esp.3290020408, 1977.

Cossart, E., Braucher, R., Fort, M., Bourlès, D., and Carcaillet, J.: Slope instability in relation to glacial debuttressing in alpine areas (Upper Durance catchment, southeastern France): Evidence from field data and 10Be cosmic ray exposure ages, Geomorphology, 95, 3–26, https://doi.org/10.1016/j.geomorph.2006.12.022, 2008.

Cruden, D. and Varnes, D.: Cruden,D.M.,Varnes, D.J.,1996, Landslide Types and Processes, Transportation Research Board, U.S. National Academy of Sciences, Special Report, 247: 36-75, Special Report - National Research Council, Transportation Research Board, 247, 36–57, 1996.

Dai, C., Higman, B., Lynett, P. J., Jacquemart, M., Howat, I. M., Liljedahl, A. K., Dufresne, A., Freymueller, J. T., Geertsema, M., Ward Jones, M., and Haeussler, P. J.: Detection and Assessment of a Large and Potentially Tsunamigenic Periglacial Landslide in Barry Arm, Alaska, Geophysical Research Letters, 47, e2020GL089 800, https://doi.org/10.1029/2020GL089800, _eprint: https://onlinelibrary.wiley.com/doi/pdf/10.1029/2020GL089800, 2020.

Deline, P., Gruber, S., Amann, F., Bodin, X., Delaloye, R., Failletaz, J., Fischer, L., Geertsema, M., Giardino, M., Hasler, A., Kirkbride, M., Krautblatter, M., Magnin, F., McColl, S., Ravanel, L., Schoeneich, P., and Weber, S.: Ice loss from glaciers and permafrost and related slope instability in high-mountain regions, in: Snow and Ice-Related Hazards, Risks, and Disasters, pp. 501–540, Elsevier, https://doi.org/10.1016/B978-0-12-817129-5.00015-9, 2021.

Dematteis, N., Giordan, D., Troilo, F., Wrzesniak, A., and Godone, D.: Ten-Year Monitoring of the Grandes Jorasses Glaciers Kinematics. Limits, Potentialities, and Possible Applications of Different Monitoring Systems, Remote Sensing, 13, 3005, https://doi.org/10.3390/rs13153005, 2021.

455 Duncan, J. M.: State of the Art: Limit Equilibrium and Finite-Element Analysis of Slopes, Journal of Geotechnical Engineering, 122, 577–596, https://doi.org/10.1061/(ASCE)0733-9410(1996)122:7(577), publisher: American Society of Civil Engineers, 1996.

Duncan, J. M.: Factors of Safety and Reliability in Geotechnical Engineering, Journal of Geotechnical and Geoenvironmental Engineering, 126, 307–316, https://doi.org/10.1061/(ASCE)1090-0241(2000)126:4(307), publisher: American Society of Civil Engineers, 2000.

Eberhardt, E., Preisig, G., and Gischig, V.: Progressive failure in deep-seated rockslides due to seasonal fluctuations in pore pressures and
460 rock mass fatigue, in: Landslides and Engineered Slopes. Experience, Theory and Practice, CRC Press, num Pages: 16, 2016.

Eriksen, H. , Rouyet, L., Lauknes, T. R., Berthling, I., Isaksen, K., Hindberg, H., Larsen, Y., and Corner, G. D.: Recent Acceleration of a Rock Glacier Complex, Ádjet, Norway, Documented by 62 Years of Remote Sensing Observations, Geophysical Research Letters, 45, 8314–8323, https://doi.org/10.1029/2018GL077605, _eprint: https://onlinelibrary.wiley.com/doi/pdf/10.1029/2018GL077605, 2018.

Fukozono, T.: Recent studies on time prediction of slope failure, Landslide News, 4, 9–12, https://cir.nii.ac.jp/crid/1570572699789681280,
465 1990.

Geertsema, M., Schwab, J. W., Blais-Stevens, A., and Sakals, M. E.: Landslides impacting linear infrastructure in west central British Columbia, Natural Hazards, 48, 59–72, https://doi.org/10.1007/s11069-008-9248-0, 2009.

Geertsema, M., Menounos, B., Bullard, G., Carrivick, J. L., Clague, J. J., Dai, C., Donati, D., Ekstrom, G., Jackson, J. M., Lynett, P., Pichierri, M., Pon, A., Shugar, D. H., Stead, D., Del Bel Belluz, J., Friele, P., Giesbrecht, I., Heathfield, D., Millard, T., Nasonova, S., Schaeffer,
470 A. J., Ward, B. C., Blaney, D., Blaney, E., Brillon, C., Bunn, C., Floyd, W., Higman, B., Hughes, K. E., McInnes, W., Mukherjee, K., and Sharp, M. A.: The 28 November 2020 Landslide, Tsunami, and Outburst Flood – A Hazard Cascade Associated With Rapid Deglaciation at Elliot Creek, British Columbia, Canada, Geophysical Research Letters, 49, https://doi.org/10.1029/2021GL096716, 2022.

Giordan, D., Dematteis, N., Allasia, P., and Motta, E.: Classification and kinematics of the Planpincieux Glacier break-offs using photographic time-lapse analysis, Journal of Glaciology, 66, 188–202, https://doi.org/10.1017/jog.2019.99, 2020.

475 Goodrich, L. E.: The influence of snow cover on the ground thermal regime, Canadian Geotechnical Journal, 19, 421–432, https://doi.org/10.1139/t82-047, 1982.

Griswold, R. and Iverson, R.: Mobility Statistics and Automated Hazard Maapping for Debris Flows and Rock Avalanches, Scientific Investigations Report 2007-5276, U.S. Geological Survey, 2008.

Hengl, T., de Jesus, J. M., MacMillan, R. A., Batjes, N. H., Heuvelink, G. B. M., Ribeiro, E., Samuel-Rosa, A., Kempen, B., Leenaars,
480 J. G. B., Walsh, M. G., and Gonzalez, M. R.: SoilGrids1km — Global Soil Information Based on Automated Mapping, PLoS ONE, 9, e105 992, https://doi.org/10.1371/journal.pone.0105992, 2014.

Huggel, C., Salzmann, N., Allen, S., Caplan-Auerbach, J., Fischer, L., Haeberli, W., Larsen, C., Schneider, D., and Wessels, R.: Recent and future warm extreme events and high-mountain slope stability, Philosophical Transactions of the Royal Society A: Mathematical, Physical and Engineering Sciences, 368, 2435–2459, https://doi.org/10.1098/rsta.2010.0078, publisher: Royal Society, 2010.

485 Ito, Y. and Ikari, M. J.: Velocity- and slip-dependent weakening in simulated fault gouge: Implications for multimode fault slip: VELOCITY-AND SLIP-DEPENDENT FRICTION, Geophysical Research Letters, 42, 9247–9254, https://doi.org/10.1002/2015GL065829, 2015.

Iverson, R. M., George, D. L., Allstadt, K., Reid, M. E., Collins, B. D., Vallance, J. W., Schilling, S. P., Godt, J. W., Cannon, C. M., Magirl, C. S., Baum, R. L., Coe, J. A., Schulz, W. H., and Bower, J. B.: Landslide mobility and hazards: implications of the 2014 Oso disaster, Earth and Planetary Science Letters, 412, 197–208, https://doi.org/10.1016/j.epsl.2014.12.020, 2015.

490   Jafarov, E. E., Marchenko, S. S., and Romanovsky, V. E.: Numerical modeling of permafrost dynamics in Alaska using a high spatial
       resolution dataset, The Cryosphere, 6, 613–624, https://doi.org/10.5194/tc-6-613-2012, 2012.

Johnson, G., Chang, H., and Fountain, A.: Active rock glaciers of the contiguous United States: geographic information system inventory
       and spatial distribution patterns, Earth System Science Data, 13, 3979–3994, https://doi.org/10.5194/essd-13-3979-2021, 2021.

Kenner, R., Phillips, M., Beutel, J., Hiller, M., Limpach, P., Pointner, E., and Volken, M.: Factors Controlling Velocity Variations at Short-
495   Term, Seasonal and Multiyear Time Scales, Ritigraben Rock Glacier, Western Swiss Alps, Permafrost and Periglacial Processes, 28,
       675–684, https://doi.org/10.1002/ppp.1953, _eprint: https://onlinelibrary.wiley.com/doi/pdf/10.1002/ppp.1953, 2017.

Kersten, M. S.: THERMAL PROPERTIES OF SOILS, vol. 52, University of Minnesota - Institute of Technology, 1949.

Kos, A., Amann, F., Strozzi, T., Delaloye, R., Ruette, J., and Springman, S.: Contemporary glacier retreat triggers a rapid landslide response,
       Great Aletsch Glacier, Switzerland, Geophysical Research Letters, 43, https://doi.org/10.1002/2016GL071708, 2016.

500   Kääb, A., Leinss, S., Gilbert, A., Bühler, Y., Gascoin, S., Evans, S. G., Bartelt, P., Berthier, E., Brun, F., Chao, W.-A., Farinotti, D., Gimbert,
       F., Guo, W., Huggel, C., Kargel, J. S., Leonard, G. J., Tian, L., Treichler, D., and Yao, T.: Massive collapse of two glaciers in western Tibet
       in 2016 after surge-like instability, Nature Geoscience, 11, 114–120, https://doi.org/10.1038/s41561-017-0039-7, number: 2 Publisher:
       Nature Publishing Group, 2018.

Labuz, J. F. and Zang, A.: Mohr–Coulomb Failure Criterion, Rock Mechanics and Rock Engineering, 45, 975–979,
505   https://doi.org/10.1007/s00603-012-0281-7, 2012.

Lacroix, P., Belart, J. M. C., Berthier, E., Sæmundsson, , and Jónsdóttir, K.: Mechanisms of Landslide Destabiliza-
       tion Induced by Glacier-Retreat on Tungnakvíslarjökull Area, Iceland, Geophysical Research Letters, 49, e2022GL098 302,
       https://doi.org/10.1029/2022GL098302, _eprint: https://onlinelibrary.wiley.com/doi/pdf/10.1029/2022GL098302, 2022.

Lipovsky, P. S., Evans, S. G., Clague, J. J., Hopkinson, C., Couture, R., Bobrowsky, P., Ekström, G., Demuth, M. N., Delaney, K. B.,
510   Roberts, N. J., Clarke, G., and Schaeffer, A.: The July 2007 rock and ice avalanches at Mount Steele, St. Elias Mountains, Yukon, Canada,
       Landslides, 5, 445–455, https://doi.org/10.1007/s10346-008-0133-4, 2008.

Milliner, C. and Donnellan, A.: Using Daily Observations from Planet Labs Satellite Imagery to Separate the Surface Deformation between
       the 4 July Mw 6.4 Foreshock and 5 July Mw 7.1 Mainshock during the 2019 Ridgecrest Earthquake Sequence, Seismological Research
       Letters, 91, 1986–1997, https://doi.org/10.1785/0220190271, 2020.

515   NPS: NPS Visitation Numbers, https://www.nps.gov/aboutus/visitation-numbers.htm, 2022.

NRCS: SNOwpack TELemetry Network (SNOTEL), https://data.nal.usda.gov/dataset/snowpack-telemetry-network-snotel, 2023.

Overeem, I., Jafarov, E., Wang, K., Schaefer, K., Stewart, S., Clow, G., Piper, M., and Elshorbany, Y.: A Modeling Toolbox for Permafrost
       Landscapes, Eos, 99, https://doi.org/10.1029/2018EO105155, 2018.

Patton, A. I., Rathburn, S. L., and Capps, D. M.: Landslide response to climate change in permafrost regions, Geomorphology, 340, 116–128,
520   https://doi.org/10.1016/j.geomorph.2019.04.029, 2019.

Pudasaini, S. P. and Krautblatter, M.: A two-phase mechanical model for rock-ice avalanches, Journal of Geophysical Research: Earth Sur-
       face, 119, 2272–2290, https://doi.org/10.1002/2014JF003183, _eprint: https://onlinelibrary.wiley.com/doi/pdf/10.1002/2014JF003183,
       2014.

Rocscience: Slide 2 2D Limit Equilibrium Slope Stability for Soil and Rock Slopes, 2021.

525   Rosen, P. A., Gurrola, E., Sacco, G. F., and Zebker, H.: The InSAR scientific computing environment, in: EUSAR 2012; 9th European
       Conference on Synthetic Aperture Radar, pp. 730–733, 2012.

Schaefer, K. and Jafarov, E.: A parameterization of respiration in frozen soils based on substrate availability, Biogeosciences, 13, 1991–2001, https://doi.org/10.5194/bg-13-1991-2016, 2016.

Scuderi, M., Collettini, C., and Marone, C.: Frictional stability and earthquake triggering during fluid pressure stimulation of an experimental

530   fault, Earth and Planetary Science Letters, 477, 84–96, https://doi.org/10.1016/j.epsl.2017.08.009, 2017.

Shan, W., Guo, Y., Wang, F., Marui, H., and Strom, A., eds.: Landslides in Cold Regions in the Context of Climate Change, Environmental Science and Engineering, Springer International Publishing, Cham, https://doi.org/10.1007/978-3-319-00867-7, 2014.

Stoffel, M. and Huggel, C.: Effects of climate change on mass movements in mountain environments, Progress in Physical Geography: Earth and Environment, 36, 421–439, https://doi.org/10.1177/0309133312441010, publisher: SAGE Publications Ltd, 2012.

535   Sturm, M., Holmgren, J., and Liston, G.: A seasonal snow cover classification system for local to global applications, Journal of Climate, 8, 1261–1283, 1995.

Team, P.: Planet Application Program Interface: In space for Life on Earth, https://api.planet.com, 2017.

USGS: National Hydrography Dataset (ver. USGS National Hydrography Dataset Best Resolution (NHD), http://prd-tnm. s3-website-us-west-2.amazonaws.com/?prefix=StagedProducts/Hydrography/NHD/HU4/HighResolution/GDB/, 2019.

540   Viesca, R. C. and Rice, J. R.: Nucleation of slip-weakening rupture instability in landslides by localized increase of pore pressure, Journal of Geophysical Research: Solid Earth, 117, https://doi.org/10.1029/2011JB008866, _eprint: https://onlinelibrary.wiley.com/doi/pdf/10.1029/2011JB008866, 2012.

Voight, B.: A Relation to Describe Rate-Dependent Material Failure, Science, 243, 200–203, https://doi.org/10.1126/science.243.4888.200, publisher: American Association for the Advancement of Science, 1989.

545   Whalley, W. B. and Martin, H. E.: Rock glaciers : II models and mechanisms, Progress in Physical Geography: Earth and Environment, 16, 127–186, https://doi.org/10.1177/030913339201600201, publisher: SAGE Publications Ltd, 1992.

Yunjun, Z., Fattahi, H., and Amelung, F.: Small baseline InSAR time series analysis: Unwrapping error correction and noise reduction, Computers & Geosciences, 133, 104 331, https://doi.org/10.1016/j.cageo.2019.104331, 2019.

Zhang, T.: Influence of the seasonal snow cover on the ground thermal regime: An overview: SNOW COVER AND GROUND THERMAL

550   REGIME, Reviews of Geophysics, 43, https://doi.org/10.1029/2004RG000157, 2005.